

Article

A Theoretical Model for the Triple Phase Boundary of Solid Oxide Fuel Cell Electrospun Electrodes

Wei Kong *, Mengtong Zhang, Zhen Han and Qiang Zhang *

School of Energy and Power, Jiangsu University of Science and Technology, Zhenjiang 212003, Jiangsu, China; 17368088830@163.com (M.Z.); hz941123@163.com (Z.H.)

* Correspondence: wkong@just.edu.cn (W.K.); qiangzhang@stu.xjtu.edu.cn (Q.Z.);
Tel.: +86-511-84417398 (W.K.); Fax: +86-511-84404433 (W.K.)

Received: 31 December 2018; Accepted: 28 January 2019; Published: 31 January 2019



Featured Application: Solid oxide fuel cells (SOFC) are one of the power-generated devices that have received much attention over the last decade due to advantages, such as a high efficiency, quietness, multiple fuels, and the inexpensive catalyst nature. To improve the performance of SOFC, the electrospun electrode is introduced to the SOFC, which can be achieved by impregnating nanoscale particles on the backbone surface of fibers. In this paper, a theoretical model was developed for the electrospun electrode. This model captures the key geometric parameters and their interrelationships, which can be used to design the microstructure parameters, such as the particle radius, fiber radius, and impregnation loading.

Abstract: Electrospinning is a new state-of-the-art technology for the preparation of electrodes for solid oxide fuel cells (SOFC). Electrodes fabricated by this method have been proven to have an experimentally superior performance compared with traditional electrodes. However, the lack of a theoretic model for electrospun electrodes limits the understanding of their benefits and the optimization of their design. Based on the microstructure of electrospun electrodes and the percolation threshold, a theoretical model of electrospun electrodes is proposed in this study. Electrospun electrodes are compared to fibers with surfaces that were coated with impregnated particles. This model captures the key geometric parameters and their interrelationship, which are required to derive explicit expressions of the key electrode parameters. Furthermore, the length of the triple phase boundary (TPB) of the electrospun electrode is calculated based on this model. Finally, the effects of particle radius, fiber radius, and impregnation loading are studied. The theory model of the electrospun electrode TPB proposed in this study contributes to the optimization design of SOFC electrospun electrode.

Keywords: solid oxide fuel cells; electrospinning; triple phase boundary; electrode

1. Introduction

Solid oxide fuel cells (SOFC) have received much attention over the last decade due to advantages, such as a high efficiency, quietness, multiple fuels, and the inexpensive catalyst nature [1–4]. One of the major challenges related to SOFCs is the short lifetime introduced by the high operating temperature. The decrease of the working temperature is an effective method to increase the lifespan of SOFC. Therefore, lower or intermediate temperature SOFC have been extensively studied in recent years [5,6]. The electrochemical reactions in the SOFC electrode only take place at the so-called triple phase boundary (TPB), where oxygen ions, electrons, and gaseous species cohere. The reaction activity of the TPB sharply decreases with decreasing temperature. Therefore, it is significant for lower or intermediate temperature SOFC to have a long TPB.

The TPB length is a critical geometric parameter of the electrode and dominates the SOFC and electrode performance [7,8]. Meanwhile, the TPB itself is strictly associated with the electrode micromorphology [9,10]. To further improve the electrode performance, many studies focused on deriving an optimal micromorphology from various fabricating processes, such as screen-printing [11,12], freeze-casting/phase inversion [13,14], co-precipitation [15], impregnation/infiltration [16,17], and electrospinning [18,19]. Several types of electrodes with distinct microstructures have been successfully prepared.

Conventional electrodes (CE), which are fabricated by sintering composite powders, have been widely and deeply studied both experimentally and theoretically. The TPB length of CE can be extracted from the detailed microstructure obtained, by focused ion beam-scanning electron microscopy (FIB-SEM) [20,21] or X-ray diffraction [22]. Theoretical models for TPB calculation can be used to systematically study the impacts of the electrode properties, including the particle size, porosity, and component fraction on the TPB length. Among those models, the random sphere packing model has become popular [23–25].

However, to improve the electrode performance or lower the operation temperature, limitations of the CE, such as the incompatible thermal expansion coefficient of the anode (e.g., Ni and yttria-stabilized zirconia (YSZ)) and high polarization loss of the cathode [26–28], have to be overcome. To address those problems, a nanostructured electrode can be introduced to the SOFC, which can be achieved by impregnating nanoscale particles on the backbone surface of another phase [16,29]. The nanostructure of the impregnated electrode (IE) leads to a tremendous enhancement of the TPB length and the impregnation phase volume fraction (e.g., Ni) is much lower than that of the CE [30]. From a phenomenological viewpoint, there are two distinct IE constituents: backbone and coated impregnation nanoparticles. These features constitute the basis of theoretical models because the IE is modeled in many cases as a sphere-packed backbone with a surface that is coated with nanospheres of another phase [26,30].

Because the TPB length of the nanostructured electrode is directly related to the total backbone surface area [31], it is logical to explore new frameworks with increased surface areas to improve the electrode performance. The basic backbone formed by many one-dimensional nanostructures (e.g., nanofibers) possesses a high surface area and porosity [32], which implies a novel backbone structure. Because electrospinning is a simple and effective method to produce uniform one-dimensional nanofibers with a high specific area and porosity, it has become a new state-of-the-art technology for the preparation of electrodes for SOFCs [33]. Li et al. [34] studied fibrous Ni-coated YSZ anodes, where the YSZ nanofibers were prepared via electrospinning and then electrolessly plated with a layer of Ni. Their results suggested that the Ni loading is only 30 wt.%, that is, lower than that of CE. Two anodes with the same Ni fraction were prepared by electrospinning and power processing, respectively. The test results showed that the peak power density of the cell with the electrospun anode is twice that obtained using the power-processing anode, which was attributed to the longer TPB of the former anode. Zhao et al. [33] compared $\text{La}_{0.8}\text{Sr}_{0.2}\text{Co}_{0.2}\text{Fe}_{0.8}\text{O}_{3-\delta}$ (LSCF) nanorod/ $\text{Ce}_{0.8}\text{Gd}_{0.2}\text{O}_{1.9}$ (GDC) nanoparticle composite cathode with LSCF/GDC nanoparticle cathode. The polarization resistance of the former is five times smaller than that of the latter. Further studies indicated that the cathode performance is better when the diameter of the nanofibers is sufficiently small [33,35]. Other studies [36,37] confirmed the significant influence of the microstructure and intrinsic properties of the basic components on the cathode performance.

Although the CE and IE have been widely studied, the electrospun electrode (EE) morphology differs from that of the CE or IE. The models and results for the CE and IE cannot be directly applied to the EE. The 3D reconstruction via FIB-SEM or X-ray diffraction is a powerful tool to quantitatively analyze the geometric properties of CEs. However, those methods cannot be used to reconstruct the impregnated microstructure due to the resolution gap [31]. Therefore, although the experimental activities are strong, as aforementioned, most experiments focused on the preparation and testing of the macro-performance; quantitative analyses of the geometric properties are rare. Contrary to in-depth

experimental studies, there is little theoretical research, to the best of our knowledge. The work of Enrico, A. and Costamagna, P [38] was developed specifically for LSCF fibers. Being LSCF a MIEC (mixed ionic electronic conductor, embedding both electronic and ionic conduction simultaneously), a number of infiltrated particles below the percolation threshold were considered. Conversely, in the present work, the fibers are considered to be a pure ionic conductor, and percolation of the infiltrated electronic conducting particles is a mandatory feature for the electrochemical reaction to expand into the electrode bulk, i.e. for the infiltration/fiber interface to contribute to the TPB. In this paper, based on the microstructure of EE reported in literatures [18,19] and the percolation threshold, a theoretical model was developed for the EE by comparing the EE to fibers with surfaces that were coated with impregnated particles. This model captures the key geometric parameters and their interrelationship, which can be used to derive explicit expressions of several key electrode parameters. Furthermore, the TPB length of the EE was calculated based on this model. Finally, the effects of the particle radius, fiber radius, and impregnation loading were systematically studied.

2. Theoretical Model

Generally, EE is fabricated by combining electrospinning and impregnation methods. The nanofibers are firstly prepared via electrospinning, followed by casting/printing on the electrolyte and co-sintering to generate the backbone. Subsequently, nanoparticles are coated on the surface of the backbone by impregnation. However, with increasing impregnation loading, the layers of the coated particles may vary from less than one layer to more than one layer.

The multiple fabrication processes of EE lead to its distinctive microstructures. From a phenomenological viewpoint, the EE is a combination of the backbone and outer shell. The backbone closely resembles the packing of straight fibers because it is fabricated by sintering electrospinning fibers. Despite the sintering, the backbone still holds the straight fiber structure [33,38]. The outer shell consists of impregnated nanoparticles, which adhere to the backbone surface. Based on the microscopic images [33,34], the nanoparticles are spherical. To simulate the heat treatment, contact angles are allowed between the spheres and between fibers and spheres.

Therefore, the backbone is considered to be a straight fiber structure in the theoretical model and the impregnated particles are considered to be spheres. In addition, all of the electrospun fibers and the impregnated particles in EE are of similar size. Thus, in order to simplify the model, the assumption that all of the electrospun fibers (the impregnated particles) have the same radii is adopted. The contact angle is widely used to describe the sintering process, which is generally set as 15° in CE and IE [29,35]. As a result, it is reasonable to assume the contact angle between particles or between fiber and particle is 15° . As we all know, in the impregnating process, the nanoparticles randomly stick to the surface of the fibers irregularly [18]. Therefore, we assume that the particles are randomly dispersed on the fiber face. In fact, fibers possess three surfaces, including the top, side, and bottom surface where the nanoparticles can stick. The intersection between the fibers covers part of the surface of the fibers. However, it is a formidable challenge for the quantitative calculation of the reduction of the fibers surface due to the intersection between the fibers. Thus, we assume that the total area of the top and bottom surface of fiber equals to the reduction of the fibers surface due to the intersection between the fibers. The nanoparticles can only stick to the side surface of the fibers in this theoretical model. In a word, the assumptions include the following:

1. All electrospun fibers have constant radii.
2. All particles have constant radii.
3. The particles are coated on the fiber face; the contact degree is 15° .
4. The contact degree between particles is 15° .
5. If the outer shell is smaller than one layer, the particles will be randomly dispersed on the fiber face.
6. The intersecting region between the fibers is neglected.

Figure 1 shows the schematic diagram of the developed theoretical model: Straight fibers (yellow cylinders) are randomly arranged in the electrode, acting as the backbone; nanoparticles (gray spheres) are coated on the fiber surfaces in three possible configurations. Depending on the impregnation loading, the shell may be smaller than one layer and one layer may be bigger (Figure 1, from left to right). For a shell, which is not smaller than one layer, the percolation ratio P^{shell} of the particles is 1. However, if the shell is smaller than one layer, the particles are randomly dispersed on the fiber face based on the fifth assumption (Figure 2a). In this case, the P^{shell} must be determined via percolation theory. Several particles cannot be connected to any of the percolation clusters (Figure 2a, red oval frame), and thus do not contribute to the TPB and need to be deleted, as shown in Figure 2b. In this paper, an algorithm was proposed to determine the P^{shell} of the shell that is smaller than one layer.



Figure 1. The schematic diagram of the theoretical model under different impregnation loadings. The shell of the impregnated particles may be smaller than one layer (left), one layer (middle), and bigger than one layer (right).

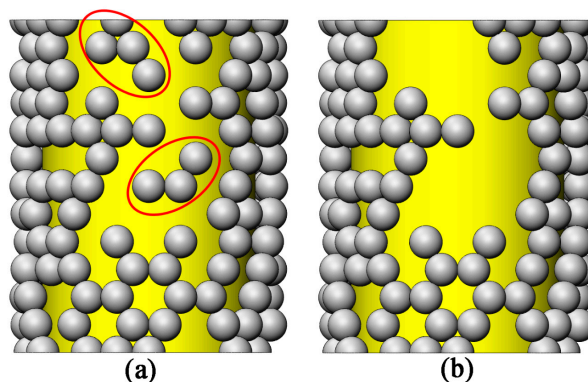


Figure 2. The schematic diagram of the case in which the shell is smaller than one layer, (a) the particles are randomly dispersed on the fiber face and some particles do not percolate in the red oval frame and (b) shows the schematic after deleting the particles that do not percolate.

3. TPB Length Calculation

For the TPB length calculation, the fiber and particle are considered to be ionic and electronic conductors, respectively. Exchanging their roles will not influence the TPB calculation because they are pure (ionic or electronic) conductors. However, the influence on the TPB of the mixed ionic and electronic conductor (MIEC) is still under discussion [39].

Figure 1 shows that the impregnated fibers are randomly distributed in the electrode. They have different lengths, positions, and orientations. Because of the different volume fraction, the number of fibers also differs. For the TPB calculation, a repeating unit is first abstracted by tailoring the impregnated fiber, as shown in Figure 3. This way, the volume-specific effective TPB length λ_{TPB}^v can be given by:

$$\lambda_{TPB}^v = 2\pi r_{el} \sin \alpha_0 \cdot Z_{io-el} n_v p_{io} p_{el} \tag{1}$$

where r_{el} are the radii of the electron-conducting particles in the shell; α_0 is the contact angle between the fibers and particles, which is 15° [40,41]; Z_{io-el} is the coordination number between the fibers and particles in the repeating unit; n_v is the number of repeating units per unit volume; p_{io} is the percolation ratio of the ion-conducting fibers; and p_{el} is the percolation ratio of the electron-conducting particles.

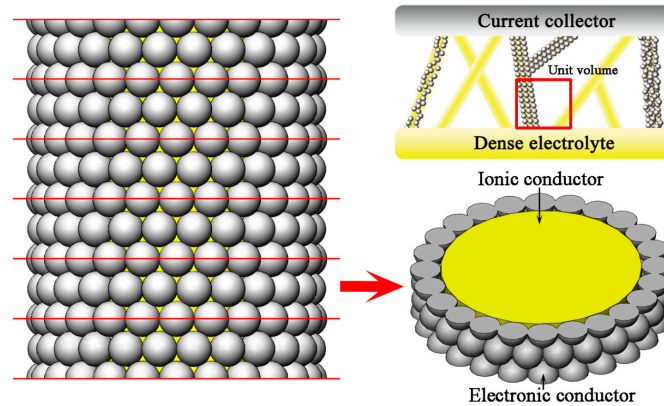


Figure 3. The schematic diagram of the repeating unit.

Based on Equation (1), the primary task of determining λ_{TPB}^v is the determination of the parameters in the equation, that is, the coordination number between the fibers and particles in the repeating unit Z_{io-el} , number of repeating units per unit volume n_v , percolation ratio of the ion-conducting fibers p_{io} , and percolation ratio of the electron-conducting particles p_{el} .

The coordination number between the fibers and particles in the repeating unit: the coordination number Z_{io-el} between the fibers and particles in the repeating unit can be geometrically derived. Figure 4 illustrates the geometric relations in the repeating unit. The coordination number is:

$$Z_{io-el} = 2 \frac{360^\circ}{\theta} \eta \tag{2}$$

where θ is the central angle of the fiber occupied by one particle (see Figure 4a). Notably, two layers of particles surround the fiber in the repeating unit, as shown in Figure 3. The parameter η is the impregnation loading, which is defined as the ratio of the total impregnated particle number, to the particle number of the one-layer case. Therefore, η is 1 in the one-layer shell case. For shells with more than one layer, η is still 1 because the particles beyond the first layer are not in contact with the fibers, and thus do not influence the TPB length. However, η is smaller than 1 in the shells that are smaller than one layer.

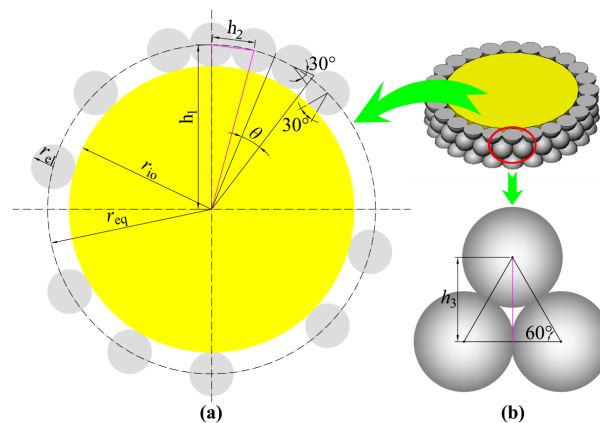


Figure 4. The schematic illustration of geometric relations in the repeating unit. (a) the define of crucial parameters. (b) the define of h_3 .

The central angle θ can be geometrically calculated by:

$$\theta = \arccos \frac{2h_1^2 - h_2^2}{2h_1^2} \quad (3)$$

where h_1 and h_2 are schematically illustrated in Figure 4, they are calculated as:

$$h_1 = \sqrt{r_{io}^2 - (r_{el} \sin \alpha_0)^2} + r_{el} \cos \alpha_0 \quad (4)$$

$$h_2 = 2 \cdot r_{el} \cos \alpha_0 \quad (5)$$

where r_{io} is the radius of the ion conducting fiber.

The number of repeating units per unit volume n_v : The volume of the ion-conducting fiber in the repeating unit is:

$$V_{fib} = 2h_3\pi r_{io}^2 \quad (6)$$

where h_3 is schematically illustrated in Figure 4, it is calculated as:

$$h_3 = 2r_{el} \cos \alpha_0 \cos 30^\circ = \sqrt{3}r_{el} \cos \alpha_0 \quad (7)$$

Therefore, the number of repeating units per unit volume n_v can be derived by:

$$n_v = \frac{V_{io}}{V_{fib}} \quad (8)$$

where V_{io} is the volume fraction of the ion conducting fibers in electrode.

Percolation ratio of ion-conducting fibers p_{io} : Based on the fabrication process and microscopic images, all ion-conducting fibers are interconnected. Therefore, the percolation ratio of the ion-conducting fibers is set to $p_{io} = 1$.

Percolation ratio of electron-conducting particles p_{el} : The percolation ratio of the electron-conducting particles depends on the impregnation layers of the shell. In shells with equal or more than one layer, all particles percolate; therefore, $p_{el} = 1$. However, if the shell is smaller than one layer, the p_{el} is obtained based on percolation theory. An algorithm was developed to automatically identify percolating particles. Because the percolated cluster must start from the top particle layer to the bottom particle layer, the algorithm starts from the top layer particles, like the green ones in Figure 5a. A loop is used to identify the clusters starting from every top layer particle. In this way, some isolated clusters will be automatically filtered out, such as the C4 and C5 in Figure 5a. The result will be all of the clusters starting from the top, as the C1, C2 and C3 shown in Figure 5b. However, not every identified cluster can stretch to the bottom of the cylinder. If a cluster contains no bottom layer particle, for example, the C2, it will be deleted. Thus, the remaining clusters are all percolated, shown as C1 and C3 in Figure 5c. The amount of the particles in those clusters divided by the total particle number in shells with one layer will be p_{el} .

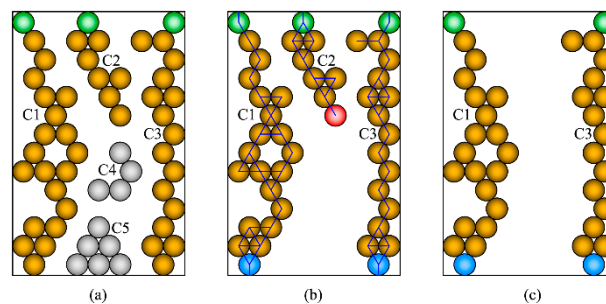


Figure 5. The schematic illustration of the algorithm of p_{el} . (a) all of the clusters. (b) all of the clusters starting from the top. (c) all the percolated clusters.

4. Results and Discussion

The TPB length of the EE was firstly calculated using our proposed theoretical model by Office Excel. Subsequently, a study was conducted to determine the effects of the impregnation loading, particle radius, and fiber radius on the TPB length. Baseline conditions were set for the parametrical study: the volume fraction of the ion-conducting fibers V_{io} is 0.45, the fiber radius is 150 nm, the particle radius is 30 nm, and $p_{el} = 1$. Unless otherwise stated, the baseline conditions were adopted.

Figure 6 shows the dependence of the percolation ratio p_{el} on the impregnation loading with different radii of the electron conducting particles r_{el} . Note that for an impregnation loading below the threshold, $p_{el} = 0$ due to no percolating particles existing. Furthermore, the threshold of the impregnation loading η increases with the increase of the r_{el} . This is because the smaller r_{el} , the more particles around the fiber, which will provide more options from the top to bottom of the fiber and form the percolated cluster. However, for an impregnation loading higher than the threshold, the percolation ratio p_{el} steeply increases. When the impregnation loading is larger than 0.66, all particles are connected for different r_{el} , that is, $p_{el} = 1$.

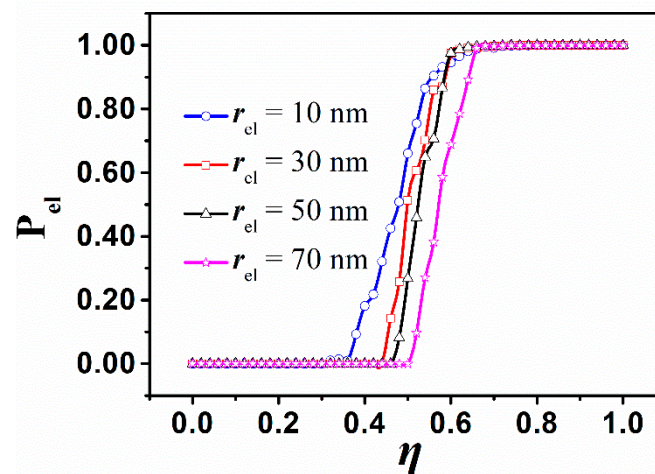


Figure 6. The dependence of the percolation ratio p_{el} on the impregnation loading.

Figure 7 shows the dependence of the TPB length on the impregnation loading. At a fixed V_{io} , particles do not percolate when the impregnation loading is too low. Thus, the effective TPB length is 0. However, when the impregnation loading reaches the threshold value of 0.48, an effective TPB begins to form and reaches for η in the range from 0.48 to 0.6, which can be attributed to the increase in the percolation ratio p_{el} and coordination number. Compared with $0.48 < \eta < 0.6$, the effective TPB length enhances relatively slowly for $\eta > 0.6$. This is due to the fact that the percolation ratio p_{el} reaches its maximum (1) at $\eta > 0.6$ and remains constant.

Figure 7 shows that the effective TPB length increases with increasing V_{io} when the impregnation loading is larger than the threshold value of 0.48. Moreover, the difference in the effective TPB length due to the change of V_{io} increases with increasing η . For example, when η is 0.5, the effective TPB length for V_{io} of 0.5 is $2.1 \times 10^{12} \text{ m}^{-1}$ higher than that for V_{io} of 0.4. However, when η is 0.6, the effective TPB length for V_{io} of 0.5 is $13.8 \times 10^{12} \text{ m}^{-1}$ higher than that for V_{io} of 0.4.

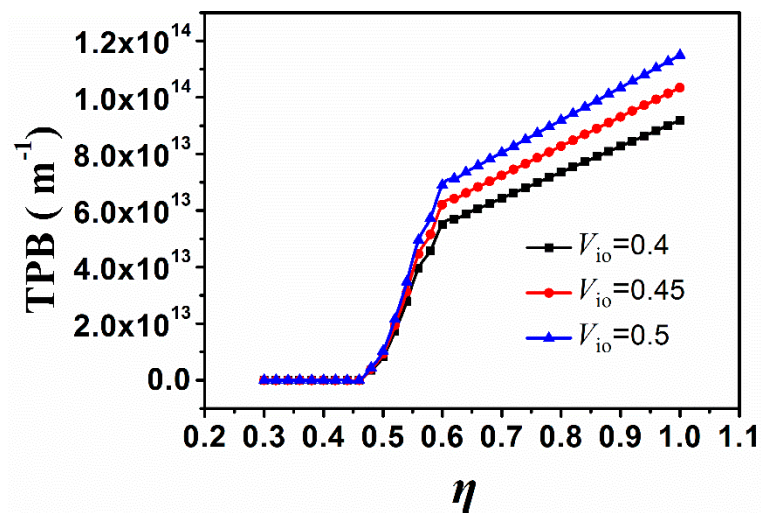


Figure 7. The dependence of triple phase boundary (TPB) length on impregnation loading.

Figure 8 shows the TPB length as a function of the electron-conducting particle radius r_{el} and ion-conducting fiber radius r_{io} with the $\eta = 1$. The TPB length of EE is high on the order of 1×10^{14} , which is close to the value of IE [30]. Note that the TPB increases with decreasing r_{el} or r_{io} . The TPB length at a r_{el} value of 30 nm only accounts for 37% of that at a r_{el} value of 10 nm for $r_{io} = 150 \text{ nm}$. However, the influence of r_{el} on the TPB length varies. For instance, at a smaller r_{el} , the TPB length drops more rapidly; at a larger r_{el} , the influence is weakened. Although finer impregnation particles are favorable for the TPB length, they can also increase the aggregation risk and directly lead to a decrease of the TPB length and bad electrode performance. In practice, the size of the impregnation particles must be carefully controlled to maximize the electrode performance.

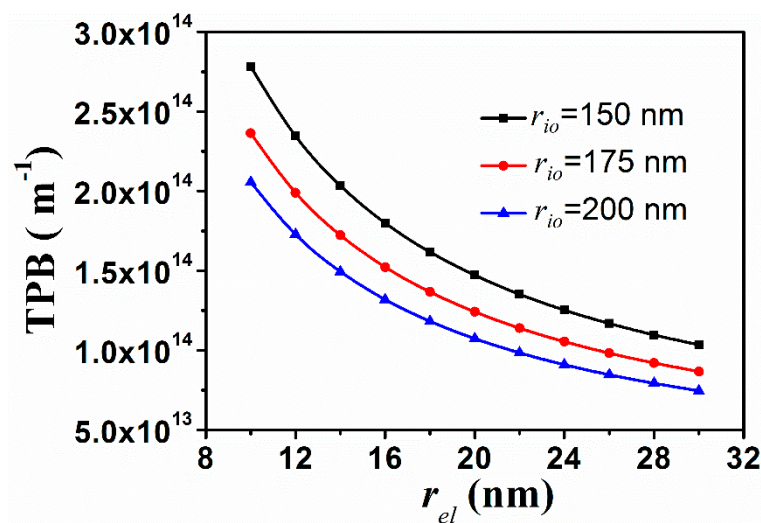


Figure 8. The dependence of TPB length on r_{el} and r_{io} .

5. Conclusions

A theoretical model was established for the electrospun electrode, which considers the fibers as cylinders and the impregnated particle as spheres. Various layers of spheres are coated on the cylinders based on different impregnation loadings. Based on this model, the TPB length of the electrospun electrode was calculated, and the effects of particle radius, fiber radius, and impregnation loading were also investigated. The results indicate that the effective TPB length difference due to the change of V_{io} increases with increasing impregnation loading η . Furthermore, thinner particle

and fiber sizes are favorable for the enhancement of the TPB length. An algorithm is developed to calculate the percolation ratio of the electron conducting particles p_{el} . It is found that the threshold of the impregnation loading η increases with the increase of the r_{el} . For an impregnation loading higher than the threshold, the percolation ratio p_{el} steeply increases. When the impregnation loading is larger than 0.66, all particles are connected for different r_{el} , that is, $p_{el} = 1$.

Author Contributions: Research articles with four authors. Methodology, W.K. and Q.Z.; software, M.Z.; validation, Z.H.; formal analysis, Z.H.; investigation, Q.Z.; resources, W.K.; data curation, M.Z.; writing—original draft preparation, Q.Z.; writing—review and editing, W.K.; visualization, M.Z.; supervision, W.K.; project administration, W.K.; funding acquisition, W.K.

Funding: This work was financially supported by the National Science Foundation of China (21406095) and the Natural Science Foundation through the Jiangsu Province General Program (BK20151325).

Conflicts of Interest: The authors declare no conflict of interest.

References

1. Irshad, M.; Siraj, K.; Raza, R.; Ali, A.; Tiwari, P.; Zhu, B.; Rafique, A.; Ali, A.; Ullah, M.K.; Usman, A. A Brief Description of High Temperature Solid Oxide Fuel Cell's Operation, Materials, Design, Fabrication Technologies and Performance. *Appl. Sci.* **2016**, *6*, 75. [[CrossRef](#)]
2. Xia, Y.; Zou, J.; Yan, W.; Li, H. Adaptive Tracking Constrained Controller Design for Solid Oxide Fuel Cells Based on a Wiener-Type Neural Network. *Appl. Sci.* **2018**, *8*, 1758. [[CrossRef](#)]
3. Chen, D.; Ding, K.; Chen, Z.; Wei, T.; Liu, K. Physics field distributions within fuel cell stacks with manifolds penetrating through the plane zone and open outlet features. *Energy Convers. Manag.* **2018**, *178*, 190–199. [[CrossRef](#)]
4. Kong, W.; Zhang, Q.; Xu, X.; Chen, D. A Simple Expression for the Tortuosity of Gas Transport Paths in Solid Oxide Fuel Cells' Porous Electrodes. *Energies* **2015**, *8*, 13953–13959. [[CrossRef](#)]
5. Jeong, D.; Kim, J.; Kwon, O.; Lim, C.; Sengodan, S.; Shin, J.; Kim, G. Scandium Doping Effect on a Layered Perovskite Cathode for Low-Temperature Solid Oxide Fuel Cells (LT-SOFCs). *Appl. Sci.* **2018**, *8*, 2217. [[CrossRef](#)]
6. Chen, D.; Hu, B.; Ding, K.; Yan, C.; Lu, L. The Geometry Effect of Cathode/Anode Areas Ratio on Electrochemical Performance of Button Fuel Cell Using Mixed Conducting Materials. *Energies* **2018**, *11*, 1875. [[CrossRef](#)]
7. Lu, Y.; Gasper, P.; Pal, U.B.; Gopalan, S.; Basu, S.N. Improving intermediate temperature performance of Ni-YSZ cermet anodes for solid oxide fuel cells by liquid infiltration of nickel nanoparticles. *J. Power Sources* **2018**, *396*, 257–264. [[CrossRef](#)]
8. Epting, W.K.; Mansley, Z.; Menasche, D.B.; Kenesei, P.; Suter, R.M.; Gerdes, K.; Litster, S.; Salvador, P.A. Quantifying intermediate-frequency heterogeneities of SOFC electrodes using X-ray computed tomography. *J. Am. Ceram. Soc.* **2017**, *100*, 2232–2242. [[CrossRef](#)]
9. Abdullah, T.; Liu, L. Simulation-based microstructural optimization of solid oxide fuel cell for low temperature operation. *Int. J. Hydrogen Energy* **2016**, *41*, 13632–13643. [[CrossRef](#)]
10. Prakash, B.S.; Kumar, S.S.; Aruna, S. Microstructure and performance of LSM/YSZ based solid oxide fuel cell cathodes fabricated from solution combustion co-synthesized powders and by solution precursor plasma spraying. *Surf. Coat. Technol.* **2017**, *310*, 25–32. [[CrossRef](#)]
11. Somalu, M.R.; Muchtar, A.; Daud, W.R.W.; Brandon, N.P. Screen-printing inks for the fabrication of solid oxide fuel cell films: A review. *Renew. Sustain. Energy Rev.* **2017**, *75*, 426–439. [[CrossRef](#)]
12. Han, D.; Liu, J.; He, Y.-B.; Wang, H.-F.; Zhang, X.-Z.; Wang, S.-R. Fabrication of a quasi-symmetrical solid oxide fuel cell using a modified tape casting/screen-printing/infiltrating combined technique. *Int. J. Hydrogen Energy* **2018**, *43*, 960–967. [[CrossRef](#)]
13. Gu, Y.; Zhang, Y.; Ge, L.; Zheng, Y.; Chen, H.; Guo, L. YSZ electrolyte support with novel symmetric structure by phase inversion process for solid oxide fuel cells. *Energy Convers. Manag.* **2018**, *177*, 11–18. [[CrossRef](#)]
14. Mousavi, A.; Niazmand, M.; Alizadeh, M. Preparation of aliened porous Ni-GDC nano composite by freeze-casting process. *Adv. Ceram. Prog.* **2017**, *3*, 10–15.

15. Dell'Agli, G.; Spiridigliozzi, L.; Marocco, A.; Accardo, G.; Frattini, D.; Kwon, Y.; Yoon, S. Morphological and crystalline evolution of Sm-(20 mol%)-doped ceria nanopowders prepared by a combined co-precipitation/hydrothermal synthesis for solid oxide fuel cell applications. *Ceram. Int.* **2017**, *43*, 12799–12808. [[CrossRef](#)]
16. Chen, J.; Wan, D.; Sun, X.; Li, B.; Lu, M. Electrochemical impedance spectroscopic characterization of impregnated $\text{La}_{0.6}\text{Sr}_{0.4}\text{Co}_{0.2}\text{Fe}_{0.8}\text{O}_{3-\delta}$ cathode for intermediate-temperature SOFCs. *Int. J. Hydrogen Energy* **2018**, *43*, 9770–9776. [[CrossRef](#)]
17. Ni, C.; Cassidy, M.; Irvine, J.T. Image analysis of the porous yttria-stabilized zirconia (YSZ) structure for a lanthanum ferrite-impregnated solid oxide fuel cell (SOFC) electrode. *J. Eur. Ceram. Soc.* **2018**, *38*, 5463–5470. [[CrossRef](#)]
18. Aruna, S.; Balaji, L.; Kumar, S.S.; Prakash, B.S. Electrospinning in solid oxide fuel cells—A review. *Renew. Sustain. Energy Rev.* **2017**, *67*, 673–682. [[CrossRef](#)]
19. Koo, J.Y.; Lim, Y.; Kim, Y.B.; Byun, D.; Lee, W. Electrospun yttria-stabilized zirconia nanofibers for low-temperature solid oxide fuel cells. *Int. J. Hydrogen Energy* **2017**, *42*, 15903–15907. [[CrossRef](#)]
20. Barnett, S.; Wang, H.; Liu, Z.; Kennouche, D.; Yakal-Kremiski, K. Imaging of Fuel Cell and Battery Electrodes Using Focused Ion Beam Scanning Electron Microscopy. *Microsc. Microanal.* **2016**, *22*, 1310–1311. [[CrossRef](#)]
21. Terao, T.; Inoue, G.; Kawase, M.; Kubo, N.; Yamaguchi, M.; Yokoyama, K.; Tokunaga, T.; Shinohara, K.; Hara, Y.; Hara, T. Development of novel three-dimensional reconstruction method for porous media for polymer electrolyte fuel cells using focused ion beam-scanning electron microscope tomography. *J. Power Sources* **2017**, *347*, 108–113. [[CrossRef](#)]
22. Johnson, T.; Bailey, J.; Iacoviello, F.; Welsh, J.; Levison, P.; Shearing, P.; Bracewell, D. Three dimensional characterisation of chromatography bead internal structure using X-ray computed tomography and focused ion beam microscopy. *J. Chromatogr. A* **2018**, *1566*, 79–88. [[CrossRef](#)] [[PubMed](#)]
23. Bertei, A.; Nicoletta, C. Percolation theory in SOFC composite electrodes: Effects of porosity and particle size distribution on effective properties. *J. Power Sources* **2011**, *196*, 9429–9436. [[CrossRef](#)]
24. Sanyal, J.; Goldin, G.M.; Zhu, H.; Kee, R.J. A particle-based model for predicting the effective conductivities of composite electrodes. *J. Power Sources* **2010**, *195*, 6671–6679. [[CrossRef](#)]
25. Zheng, K.; Ni, M. Reconstruction of solid oxide fuel cell electrode microstructure and analysis of its effective conductivity. *Sci. Bull.* **2016**, *61*, 78–85. [[CrossRef](#)]
26. Chen, M.; Song, C.; Lin, Z. Property models and theoretical analysis of novel solid oxide fuel cell with triplet nano-composite electrode. *Int. J. Hydrogen Energy* **2014**, *39*, 13763–13769. [[CrossRef](#)]
27. Kong, W.; Zhang, W.; Zhang, S.; Zhang, Q.; Su, S. Residual stress analysis of a micro-tubular solid oxide fuel cell. *Int. J. Hydrogen Energy* **2016**, *41*, 16173–16180. [[CrossRef](#)]
28. Kong, W.; Zhang, W.; Huang, H.; Zhang, Y.; Wu, J.; Xu, Y. Analysis of micro-tubular SOFC stability under ambient and operating temperatures. *J. Mater. Sci. Technol.* **2018**, *34*, 1436–1440. [[CrossRef](#)]
29. Shao, L.; Wang, P.; Zhang, Q.; Fan, L.; Zhang, N.; Sun, K. Nanostructured CuCo_2O_4 cathode for intermediate temperature solid oxide fuel cells via an impregnation technique. *J. Power Sources* **2017**, *343*, 268–274. [[CrossRef](#)]
30. Vijay, P.; Tadé, M.O.; Shao, Z.; Ni, M. Modelling the triple phase boundary length in infiltrated SOFC electrodes. *Int. J. Hydrogen Energy* **2017**, *42*, 28836–28851. [[CrossRef](#)]
31. Zhang, Y.; Sun, Q.; Xia, C.; Ni, M. Geometric Properties of Nanostructured Solid Oxide Fuel Cell Electrodes. *J. Electrochem. Soc.* **2013**, *160*, F278–F289. [[CrossRef](#)]
32. Hochbaum, A.I.; Yang, P. Semiconductor Nanowires for Energy Conversion. *Chem. Rev.* **2010**, *110*, 527–546. [[CrossRef](#)] [[PubMed](#)]
33. Zhao, E.; Jia, Z.; Zhao, L.; Xiong, Y.; Sun, C.; Brito, M.E. One dimensional $\text{La}_{0.8}\text{Sr}_{0.2}\text{Co}_{0.2}\text{Fe}_{0.8}\text{O}_{3-\delta}/\text{Ce}_{0.8}\text{Gd}_{0.2}\text{O}_{1.9}$ nanocomposite cathodes for intermediate temperature solid oxide fuel cells. *J. Power Sources* **2012**, *219*, 133–139. [[CrossRef](#)]
34. Li, L.; Zhang, P.; Liu, R.; Guo, S.M. Preparation of fibrous Ni-coated-YSZ anodes for solid oxide fuel cells. *J. Power Sources* **2011**, *196*, 1242–1247. [[CrossRef](#)]
35. Sacanell, J.; Leyva, A.G.; Bellino, M.G.; Lamas, D.G. Nanotubes of rare earth cobalt oxides for cathodes of intermediate-temperature solid oxide fuel cells. *J. Power Sources* **2010**, *195*, 1786–1792. [[CrossRef](#)]

36. Zhao, E.; Ma, C.; Yang, W.; Xiong, Y.; Li, J.; Sun, C. Electrospinning $\text{La}_{0.8}\text{Sr}_{0.2}\text{Co}_{0.2}\text{Fe}_{0.8}\text{O}_{3-\delta}$ tubes impregnated with $\text{Ce}_{0.8}\text{Gd}_{0.2}\text{O}_{1.9}$ nanoparticles for an intermediate temperature solid oxide fuel cell cathode. *Int. J. Hydrogen Energy* **2013**, *38*, 6821–6829. [[CrossRef](#)]
37. Lanzini, A.; Guerra, C.; Leone, P.; Santarelli, M.; Smeacetto, F.; Fiorilli, S.; Gondolini, A.; Mercadelli, E.; Sanson, A.; Brandon, N. Influence of the microstructure on the catalytic properties of SOFC anodes under dry reforming of methane. *Mater. Lett.* **2016**, *164*, 312–315. [[CrossRef](#)]
38. Enrico, A.; Costamagna, P. Model of infiltrated $\text{La}_{1-x}\text{Sr}_x\text{Co}_{1-y}\text{Fe}_y\text{O}_{3-\delta}$ cathodes for intermediate temperature solid oxide fuel cells. *J. Power Sources* **2014**, *272*, 1106–1121. [[CrossRef](#)]
39. Chen, D.; He, H.; Zhang, D.; Wang, H.; Ni, M. Percolation Theory in Solid Oxide Fuel Cell Composite Electrodes with a Mixed Electronic and Ionic Conductor. *Energies* **2013**, *6*, 1632–1656. [[CrossRef](#)]
40. Kong, W.; Gao, X.; Liu, S.; Su, S.; Chen, D. Optimization of the interconnect ribs for a cathode-supported solid oxide fuel cell. *Energies* **2014**, *7*, 295–313. [[CrossRef](#)]
41. Su, S.; Zhang, Q.; Gao, X.; Periasamy, V.; Kong, W. Effects of changes in solid oxide fuel cell electrode thickness on ohmic and concentration polarizations. *Int. J. Hydrogen Energy* **2016**, *41*, 16181–16190. [[CrossRef](#)]



© 2019 by the authors. Licensee MDPI, Basel, Switzerland. This article is an open access article distributed under the terms and conditions of the Creative Commons Attribution (CC BY) license (<http://creativecommons.org/licenses/by/4.0/>).